The Astrophysical Journal Letters, 970:L18 (12pp), 2024 July 20 https://doi.org/10.3847/2041-8213/ad5da4

Probing the Shock Breakout Signal of SN 2024ggi from the Transformation of Early Flash Spectroscopy

Jujia Zhang[1,2,3], Luc Dessart[4], Xiaofeng Wang[5], Qian Zhai[1,3], Yi Yang[5,6], Liping Li[1,2,3], Han Lin[1,2,3], Giorgio Valerin[7], Yongzhi Cai[1,2,3], Zhen Guo[8,9,10], Lingzhi Wang[11], Zeyi Zhao[1,2,3], Zhenyu Wang[1,2,3], and Shengyu Yan[5]
[1] Yunnan Observatories (YNAO), Chinese Academy of Sciences (CAS), Kunming, 650216, People's Republic of China; jujia@ynao.ac.cn
[2] International Centre of Supernovae, Yunnan Key Laboratory, Kunming 650216, People's Republic of China
[3] Key Laboratory for the Structure and Evolution of Celestial Objects, CAS, Kunming, 650216, People's Republic of China
[4] Institut d'Astrophysique de Paris, CNRS-Sorbonne Université, 98 bis boulevard Arago, F-75014 Paris, France
[5] Physics Department, Tsinghua University, Beijing, 100084, People's Republic of China
[6] Department of Astronomy, University of California, Berkeley, CA 94720-3411, USA
[7] INAF-Osservatorio Astronomico di Padova, Vicolo dell'Osservatorio 5, 35122 Padova, Italy
[8] Instituto de Física y Astronomía, Universidad de Valparaíso, ave. Gran Bretaña, 1111, Casilla 5030, Valparaíso, Chile
[9] Centre for Astrophysics Research, University of Hertfordshire, Hatfield AL10 9AB, UK
[10] Millennium Institute of Astrophysics, Nuncio Monseñor Sotero Sanz 100, Of. 104, Providencia, Santiago, Chile
[11] Chinese Academy of Sciences South America Center for Astronomy (CASSACA), National Astronomical Observatories, CAS, Beijing, People's Republic of China
Received 2024 June 11; revised 2024 June 27; accepted 2024 June 27; published 2024 July 19

Abstract

We present early-time, hour-to-day cadence spectroscopy of the nearby Type II supernova (SN II) 2024ggi, which was discovered at a phase when the SN shock had just emerged from the red supergiant (RSG) progenitor star. Over the first few days after the first light, SN 2024ggi exhibited prominent narrow emission lines formed through intense and persistent photoionization of the nearby circumstellar material (CSM). In the first 63 hr, spectral lines of He, C, N, and O revealed a rapid rise in ionization as a result of the progressive sweeping up of the CSM by the shock. The duration of the IIn-like spectra indicates a dense and relatively confined CSM distribution extending up to $\sim 4 \times 10^{14}$ cm. Spectral modeling reveals that a CSM mass-loss rate at this region exceeding $5 \times 10^{-3}\,M_{\odot}\,\mathrm{yr}^{-1}$ is required to reproduce low-ionization emissions, which dramatically exceeds that of an RSG. Analyzing the Hα emission shift implies the velocity of the unshocked outer CSM to be between 20 and 40 km s^{-1}, matching the typical wind velocity of an RSG. The differences between the inner and outer layers of the CSM and an RSG progenitor highlight a complex mass-loss history before the explosion of SN 2024ggi.

Unified Astronomy Thesaurus concepts: Type II supernovae (1731); Supernovae (1668); Core-collapse supernovae (304)

Materials only available in the online version of record: data behind figure

1. Introduction

Type II supernovae (SNe), characterized by the presence of prominent hydrogen features in their spectra (Filippenko 1997; Gal-Yam 2017), are the death throes of most massive stars (e.g., red supergiants, RSGs, Heger et al. 2003). A fraction of SNe II exhibit interaction signatures with circumstellar material (CSM), characterized by narrow optical emission lines with broad electron-scattering wings classified as Type IIn SNe (Niemela et al. 1985; Schlegel 1990). Some of the diversity of SNe IIn lies in the duration of the interaction signatures, which can range from a few days (e.g., SN 2013fs; Yaron et al. 2017) to several weeks (e.g., SN 1998S; Leonard et al. 2000; Chugai 2001; Fassia et al. 2001; Shivvers et al. 2015; Dessart et al. 2016), months (e.g., SN 2010jl; Zhang et al. 2012; Fransson et al. 2014), and even a few years (e.g., SN 2015da; Tartaglia et al. 2020). This indicates a range in spatial scales and mass for the CSM around their progenitor stars.

These cataclysmic events provide a unique window into the final stages of stellar evolution, especially the mass-loss history and the environment surrounding the progenitor stars. The mass-loss rates deduced from SN observations often differ from those derived from studies of RSGs in their quiescent phases, underscoring the gaps in our understanding of late-stage stellar evolution.

For example, the variety of SNe II with short-lived IIn-like spectral features, as witnessed in SNe like SN 2013fs (Dessart et al. 2017, referred to as D17 hereafter; Yaron et al. 2017), SN 2014G (Terreran et al. 2016), SN 2017ahn (Tartaglia et al. 2021), SN 2018zd (Zhang et al. 2020; Hiramatsu et al. 2021), SN 2020pni (Terreran et al. 2022), SN 2020tlf (Jacobson-Galán et al. 2022), and the recent SN 2023ixf (e.g., Bostroem et al. 2023; Hiramatsu et al. 2023; Smith et al. 2023; Zhang et al. 2023; Zimmerman et al. 2024), reveals the diversity of CSM structures and the mass-loss histories of that subset of SNe and their associated massive star progenitors. Quantitative studies show that over 30% of SNe II exhibit these transient IIn-like features (e.g., Bruch et al. 2021, 2023; Jacobson-Galán et al. 2024a), suggesting that such mass-loss events are common in massive stars about to explode, with certain SNe displaying intermediate properties between regular SNe II and strongly interacting SNe IIn.

Moreover, the early IIn-like spectra resulting from ionizations of CSM by shock photons provide a way to investigate the initial shock breakout (SBO) signal of SN explosion. The earliest emission of electromagnetic radiation from an SN

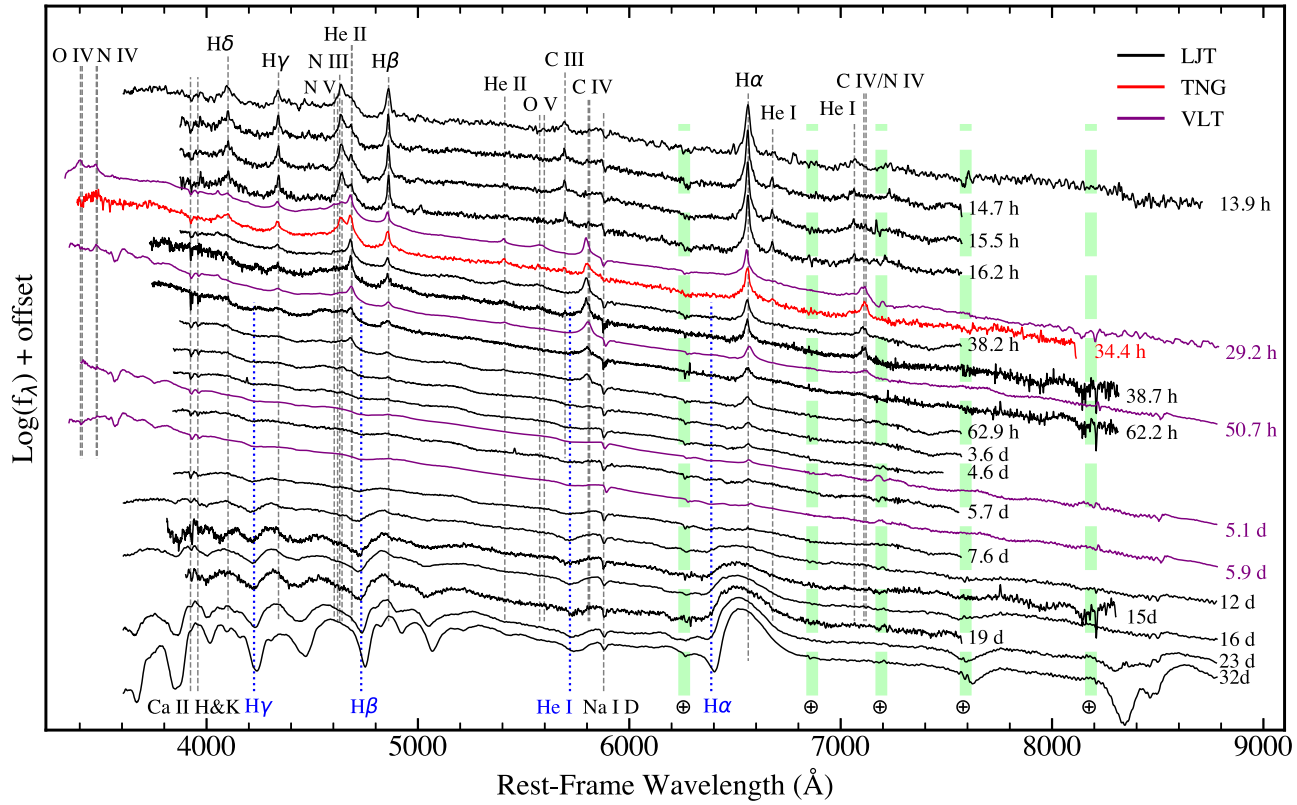

Figure 1. Spectral evolution of SN 2024ggi. Dashed gray lines indicate the rest-frame wavelengths of spectral features, while dotted blue lines represent a blueshift of -8000 km s^{-1}. Artifacts resulting from the incomplete removal of telluric absorption and skyline emissions are identified by dashed–dotted green lines, with each marked with an Earth symbol indicating the terrestrial origin. Details of the observations, including dates and conditions, are given in Table A1. The spectra are provided in machine-readable format as Data behind the Figure and can be downloaded.

(The data used to create this figure are available in the online article.)

explosion is associated with SBO, a brief yet brilliant event signifying the transition from an opaque to a transparent state as the expanding shock wave reaches the stellar surface (Waxman & Katz 2017). Once the shock approaches the progenitor (within an optical depth of $\tau \sim 10$–30), radiation begins to leak from the shock, initiating the ionization of the cool atmosphere and environment of the RSG.

The ionization process, occurring on timescales from seconds to tens of minutes, is marked by a UV flash (Waxman & Katz 2017). It is followed by UV and optical emissions from the cooling envelope. However, if there is an optically thick CSM or dust shell, the SBO might occur within this shell, and the shock emission will be reddened and prolonged, as seen in SN 2023ixf (Bostroem et al. 2023; Li et al. 2024; Zimmerman et al. 2024).

In this Letter, we present the spectroscopic observations of a nearby SN II in NGC 3621, which provides another chance to detect the SBO signals. SN 2024ggi was discovered by the Asteroid Terrestrial-impact Last Alert System (Chen et al. 2024a; Tonry et al. 2024) on 2024 April 11.14 (UTC dates are used throughout this Letter) in the nearby galaxy NGC 3621, located at a distance of $D = 7.0 \pm 0.2$ Mpc (based on the averaged Cepheid distance derived by different period–luminosity relations presented in Kanbur et al. 2003). The archive images taken with the Hubble Space Telescope about 20 yr before the explosion reveal an RSG progenitor with a temperature $T_\star = 3290^{+19}_{-27}$ K and radius $R_\star = 887^{+60}_{-51}\,R_\odot$ (Xiang et al. 2024). With the first-light date at MJD $= 60411.03 \pm 0.05$ determined through high-cadence photometric observations (S. Yan et al. 2024, in preparation), SN 20024ggi stands out as an SN II with extremely early photometric and spectroscopic observations (Tonry et al. 2024; Zhai et al. 2024).

2. Spectral Observation

2.1. Classification

Utilizing the Li-Jiang 2.4 m telescope (LJT; Fan et al. 2015) equipped with the Yunnan Faint Object Spectrograph and Camera (YFOSC; Wang et al. 2019), we obtained a classification spectrum for SN 2024ggi at ∼13.9 hr after its explosion (Zhai et al. 2024). This classification spectrum was predominantly characterized by narrow emission lines of H, He, and CNO elements, as seen in Figure 1. These features, also known as flash features (Gal-Yam et al. 2014), are commonly observed in SNe IIn (e.g., SN 1998S; Leonard et al. 2000). They are generated by recombinations of the surrounding dense CSM that is photoionized by radiation from the embedded shock.

Interestingly, in the initial-phase spectrum, SN 2024ggi exhibits a significant difference from other SNe II-P/CSM events like SN 2013fs, SN 2018zd, and SN 2023ixf. As presented in Figure 2(a), the classification spectrum of SN 2024ggi lacks the strong emission features of high-ionization states. It showed lines of He I, N III, and C III rather than those of He II, N V, and C IV or the highly ionized O V $\lambda\lambda$5576, 5598 and N V $\lambda\lambda$4604, 4620 lines that appeared in SN 2013fs.

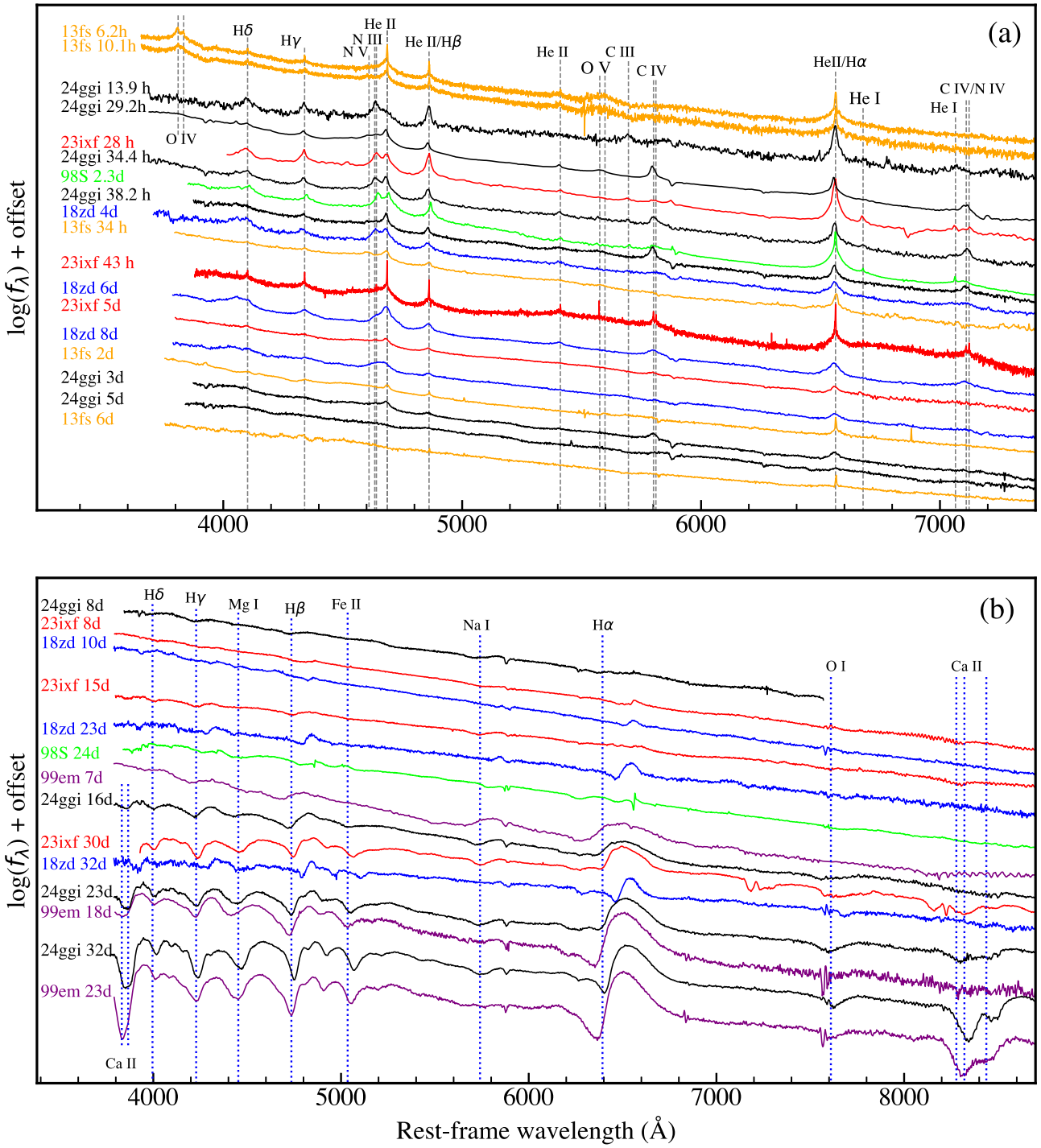

Figure 2. Spectral comparison between SN 2024ggi and the representative SNe II. (a) Flash spectroscopy of SN 2024ggi, compared with those of SN 1998S (Leonard et al. 2000; Fassia et al. 2001; Shivvers et al. 2015), SN 2013fs (Yaron et al. 2017), SN 2018zd (Zhang et al. 2020), and SN 2023ixf (Zhang et al. 2023). (b) Postflash spectra of SN 2024ggi, compared with those from SN 1998S, SN 1999em (Hamuy et al. 2001; Leonard et al. 2002; Dessart & Hillier 2006), SN 2018zd, and SN 2023ixf. The extinction correction was applied to each spectrum for which the extinction of SN 2024ggi is derived in Appendix A.2, while the extinction values of the comparisons are adopted from the lectures. Dashed gray lines represent the rest-frame wavelengths of spectral features, while the dotted blue lines represent a blueshift of -8000 km s^{-1} in velocity space.

In particular, SN 2024ggi and SN 2013fs exhibit two opposite spectral line morphologies in the 4600–4700 Å region. The spectra of SN 2013fs at $t \leqslant 10$ hr (where t denotes time after the first light) show a narrow He II λ4686 emission line, while the nearby N III $\lambda\lambda$4630, 4641 doublets appear flatter without prominent narrow-line components. Instead, there is a small bump consisting of N V $\lambda\lambda$4604, 4620. However, the classification spectrum of SN 2024ggi reveals narrow emission lines of N III $\lambda\lambda$4630, 4641, while the position corresponding to He II λ4686 appears flat. These two SNe belong to those with the earliest discoveries among the sample of SNe II-P with CSM. Spectroscopic data from other samples, usually obtained one day after the SBO, did not show similar phenomena, suggesting a high dependency of early-time spectra on the exact postbreakout epoch and the CSM properties.

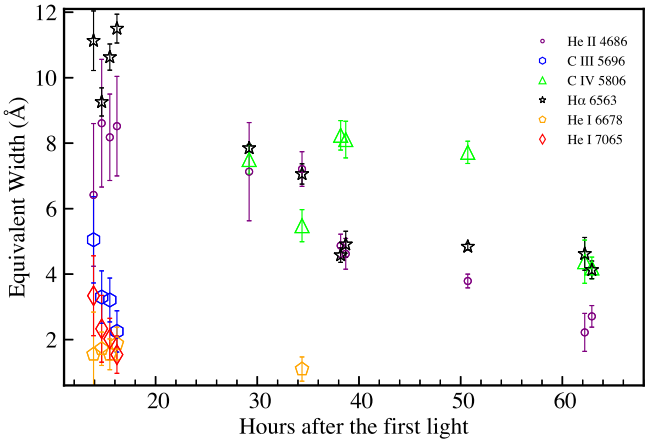

Figure 3. EW evolution of the ionization line in SN 2024ggi at $t < 3$ days. C IV 5806 is the abbreviation of C IV $\lambda\lambda$5801, 5811.

2.2. High-cadence Sampling within the Initial 72 hr

Given the observed IIn-like features in the classification spectrum and a relatively lower ionization state revealed by these features, we initiated an hour-cadence observation campaign with the LJT. A total of four spectra were acquired within 2.4 hr after the identification, which allowed us to monitor possible variations in the ionization state for this young SN II.

From the second spectrum, SN 2024ggi exhibited narrow He II λ4686 emission that was absent before. It is possible that, in the first spectrum, the CSM has not been shocked enough to generate sufficient heat for emitting a significant amount of He II, except for the deep CSM near the shock, where the material could be rushing. The subsequent two spectra did not show significant morphological evolution. Further analysis of the equivalent widths (EWs) of the main spectral lines, as shown in Figure 3, reveals that within the 1.5 hr from $t \sim 14.7$ to $t \sim 16.2$ hr, the strength of the He II λ4686 and He I λ6678 lines remained almost unchanged. In contrast, the C III λ5696 and He I λ7065 lines became gradually weak.

On the second day after explosion, an observation relay across different time zones was conducted with LJT, Telescopio Nazionale Galileo (TNG), and Very Large Telescope Unit 1 (VLT UT1), which allowed continuous monitoring of the rapid evolution of SN 2024ggi. In particular, to examine the structure of narrow spectral lines, we utilized the cross-dispersion capability of YFOSC with a resolution of 3500. This resolution had proven its effectiveness in our previous research of SN 2023ixf, enabling us to discern the intricate structure of Hα and provide a more precise constraint on its broadening (Zhang et al. 2023).

Nonetheless, in the case of SN 2024ggi, the Hα line had already undergone significant broadening in the spectra taken at $t \sim 38.7$ hr, with a full width at half-maximum (FHWM) of $\sim$700 km s^{-1}, exceeding the instrumental FWHM (i.e., $\sim$85 km s^{-1}). Concurrently, as the narrow line broadened swiftly, its EW declined steeply at $t \gtrsim 30$ hr, as illustrated in Figure 3.

The rapid broadening and decreasing of the Hα narrow component testifies to the rapid spectral evolution of SN 2024ggi. By $t \sim 29$ hr, many highly ionized spectral lines emerged in the spectrum, including O IV, N IV, C IV, and even O V. Due to limitations in the signal-to-noise ratio of the spectrum, the He II λ 5411 line can only be marginally detected at $t < 1$ day, but it becomes visible at $t \sim 29$ hr. The most notable change is that 1 day after explosion, the emission lines of He I λ7065 and C III λ5696 disappeared in the spectra but were replaced by the C IV $\lambda\lambda$5801, 5811, C IV λ7110, and N IV λ7122 lines. As shown in Figure 3, He II λ4686 continues to weaken throughout the day, while C IV $\lambda\lambda$5801, 5811 progressively gains strength. We notice that the narrow He I λ6678 line disappeared at 29.2 hr, but it reappeared 5 hr later. The He I λ5876 line is not detected, perhaps due to the fact that it coincides with the Na I D absorption of the Milky Way.

At $t \sim 29$ hr, the spectral line flux and profile morphology in this region are unreliable due to a saturation in the wavelength range from $\sim$4610 to $\sim$4700 Å. Therefore, we cannot confirm whether the appearance of N V at this time is genuine, nor can we ascertain the reliability of the intensity contrast between N III and He II. At $t \sim 34$ hr, the narrow lines of He II λ4686 and N III $\lambda\lambda$4630, 4641 have comparable intensities and thus formed a double-peak profile. Such a double-peak structure has also been seen in some SNe II. For instance, it appeared in SN 2023ixf at $t \sim 1.2$ days, SN 1998S at $t \sim 2.3$ days, and SN 2018zd at $t \sim 4$ days. SN 2013fs may also exhibit a similar structure at $t \sim 1.4$ days, except that the left peak corresponds to N V $\lambda\lambda$4604, 4620 instead of N III in its spectrum (D17; Yaron et al. 2017). The N V doublet is also visible in the spectra of SN 2024ggi taken at $t = 29.2$ hr, 38.3 hr, and 38.7 hr. This indicates that SN 2013fs and SN 2024ggi can reach similar ionization levels, though they may have different shock emissions and CSM environments.

At $t > 38$ hr, the N III doublet becomes weaker than He II λ4686 in SN 2024ggi. However, the N III doublet remains unchanged over the following days, while He II shows a faster decline in intensity. Overall, all narrow emission lines become less distinct after the third day, as they broaden significantly with a velocity exceeding 1000 km s^{-1}. The disappearance of narrow emission lines indicates that the IIn-like phase is ending and SN 2024ggi is gradually entering a new stage of evolution.

The rapid spectral evolution relates in part to a temperature change. We can roughly estimate the temperature of the SN photosphere through fits to the spectral energy distribution (SED) assuming a blackbody emission. In Figure A1, the temperature of SN 2024ggi is inferred to be about 13,500 K during the phase from 13.9 to 16.2 hr, and it increases sharply from $\sim$13,500 to $\sim$26,000 K about half a day later (also reported by Chen et al. 2024b). The rapid temperature rise is concomitant with the rapid increase in ionization, and both are attributed to the photoionizing radiation from the shock.

2.3. Flash-to-photospheric Phase Transition

Since SN 2024ggi exhibited a rapid evolution, we maintained frequent monitoring until the third day, gradually tapering off the pace after that. As presented in Figure 1, we can only see a few weak "narrow" emission lines, such as Hα and the N III $\lambda\lambda$4634, 4641 doublet at $\sim$3.6 days. Meanwhile, P Cygni profiles of Hβ, Hγ, and He I λ5876 begin to emerge.

At 3 days $< t <$ 15 days, the spectral lines of SN 2024ggi undergo a significant transition. Initially, these lines exhibited broadening due to electron scattering formed within the unshocked CSM. However, they gradually shift to Doppler broadening, as they initially formed within the fast-moving dense shell and subsequently also arise from the ejecta as the dense shell gradually becomes optically thinner. This evolution

is accompanied by a noticeable blueshift in their emission peaks. Additionally, these lines begin to appear as P Cygni profiles, with both absorption and emission components increasing in strength over time.

Roughly 2 weeks after the explosion, SN 2024ggi developed spectral features typical of SNe IIP in both optical and near-infrared (NIR) spectra, i.e., the appearance of broad H I and He I lines. For example, as seen in Figure A2, the NIR spectrum of SN 2024ggi, obtained with the 6.5 m Magellan telescope equipped with Folded-port InfraRed Echellette (FIRE) at $t \sim 14$ days, reveals similar spectral features as seen in SN 2017eaw (Szalai et al. 2019).

As observed in SN 2018zd (Zhang et al. 2020) and SN 2023ixf (Zhang et al. 2023), the SN–CSM interaction creates a slow evolution in spectral features after the narrow, electron-scattering broadened emission lines disappear (Figure 2). During shock-wave propagation, the CSM is shocked and compressed into a dense shell, converting a fraction of kinetic energy into thermal energy and heating the CSM as well as boosting the SN luminosity. In the case of SN 2024ggi, photoionization predominantly facilitates this heating process within the first 3 days. Consequently, emission from the postshock gas, such as the cold dense shell (CDS), originates from the release of shock-deposited energy (i.e., deposited at earlier times). The relatively faint spectral lines observed approximately 5 days later are likely attributed to the spectrum primarily forming within the CDS during this period. This weak emission is indicative of a steep density gradient of the CDS (D17).

We note that the evolution speed of the photospheric features in SN 2024ggi is slower than that of the typical SN 1999em but still faster than that in SN 2018zd and SN 2023ixf. As illustrated in Figure 2(b), SN 2024ggi evolves into spectra with prominent P Cygni profiles at around $t \sim 23$ days, and its spectrum at $t \sim 32$ days shows a close resemblance to that of a regular SN IIP. Nevertheless, SN 2024ggi evolves faster in the first month, regardless of early IIn or later photospheric spectra, compared to SN 2018zd and SN 2023ixf, suggesting a more compact CSM.

3. Insights into the Early Flash Spectroscopy

3.1. Fluctuation of Ionization States

Within the initial 72 hr after the first light, we obtained a total of 12 spectra revealing rapid evolution of line strengths, in particular for lines associated with different ionization levels (e.g., He I versus He II). During this period, the lower-ionization species (such as He I, C III, and N III) gradually weakened and disappeared, while the strength of emission lines from higher-ionization species (like He II, N IV, and C IV) increased (see also Section 2.2).

The evolution of these line fluxes or EWs is, however, more complex. Spectral lines such as He I λ6678, He I λ7065, and C III λ5696 disappeared at $t \sim 29.2$ hr, while higher-ionization lines, including C IV $\lambda\lambda$5801, 5811 and O V $\lambda\lambda$5576, 5598, emerged. However, 5 hr later, He I λ6678 reappeared, while O V became more elusive. In the 38.3 hr and 38.4 hr spectra, roughly 4 hr afterward, He I λ6678 vanished once again and O V reappeared, while N III significantly diminished and N V became detectable.

The weakening of N III and the emergence of N V were already evident in the 29.2 hr spectrum. Considering the evolution of O V and He I, we believe the relative intensities of N V and N III observed at 29.2 hr are reliable despite the detector saturation in this wavelength region. Thus, we observed a decreasing and increasing ionization across the 29.2, 34.4, and 38.3 hr spectra.

This trend is mirrored in Figure 3, where a similar fluctuation in C IV $\lambda\lambda$5801, 5811 is apparent in the $t \sim 30$ hr spectrum. These variations suggest that although the ionization evolution initially arose and fell within the first 72 hr, there were fluctuations when the ionization reached its maximum at around 30 hr after the first light. These fluctuations are probably related to the complicated propagation through a clumpy and perhaps asymmetric CSM. The alteration in the ionization state indicates the complex interaction between the shock wave, the surrounding material, and the high-energy radiation environment in the early stages of the SN explosion.

3.2. Comparison with Spectra Model

To further understand the evolution of the ionization state of SN 2024ggi, we compare the observed spectra with the spectral models presented in D17(as shown in Figure 4). This model set successfully reproduces the observational manifestations of SNe II, specifically those featuring short-lived IIn-like spectra, while taking into account the varying physical conditions of the progenitor before the explosion. The methodology adopted in D17 involves creating a comprehensive grid of models for different CSM characteristics (including radius, mass, density, density profile, velocity, and composition) based on the same progenitor and explosion parameters, thereby encompassing a wide range of the parameter space.

Although none of the models in D17 can fully reproduce all of the spectral features, models like r1w5r and r1w6 provide a good reference for us to track and study the ionization state and evolution of the CSM. In comparison, we found that the r1w5r model fits the observations well, especially at $t \sim 1.5$ days, when it can reproduce all the observed characteristics of SN 2024ggi. Moreover, at $t \sim 1.17$ days, high-ionization lines such as O IV and N IV appeared in the model spectrum, which is comparable to the spectrum of SN 2024ggi at $t \sim 1.35$ days, indicating that the ionization state of SN 2024ggi is consistent with the model during this period. However, the CSM in the r1w5r model has a higher ionization state at $t < 1$ day than that observed in SN 2024ggi. For example, the r1w5r model does not show an He I line in the early stage, and in fact, no He I line appears in any of the D17 models.[12] In contrast, the He II line in the r1w5r model is much stronger than the N III line at the beginning of the explosion.

Interestingly, the blue edge of Hα is quite similar in the $t \sim 16$ spectrum of SN 2024ggi and the $t = 15$ days r1w5r model spectrum. The only difference lies in the emission strength and the extent of the profile to the red. One reason might be that in the model, the optical depth attenuation is much more significant, which suggests that the CDS breaks up and becomes significantly clumpy. This could be resolved if the CDS was allowed to break up, as would occur in three-

[12] The reason is partly because no model was computed during the earliest epochs, when the first radiation from the shock was crossing the CSM (i.e., the radiative precursor). Modeling this phase is quite challenging, and there are inconsistencies in the physics addressed in D17. One such inconsistency relates to the light travel time effect, considered in radiation-hydrodynamics calculations but omitted during the postprocessing phase of radiative transfer calculations for spectra.

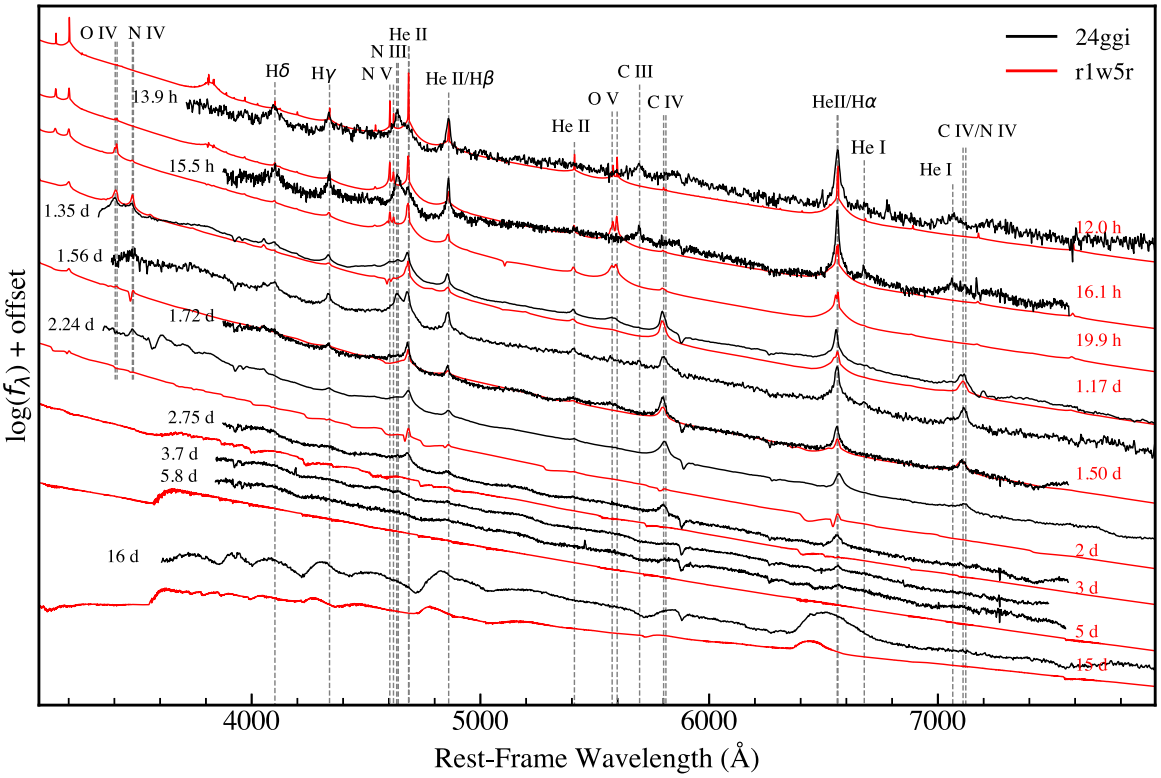

Figure 4. Comparison of early-time spectra from SN 2024ggi from 14 hr until 15 days postexplosion with the r1w5r model spectra of D17. Dashed gray lines represent the rest-frame wavelengths of spectral features. In the r1w5r model, the progenitor star radius is $R_\star = 501\,R_\odot$, the wind mass-loss rate is $\dot{M} = 5.0 \times 10^{-3}\,M_\odot\ \mathrm{yr}^{-1}$, and the outer radius of the dense CSM is $R_{\mathrm{CSM}} = 5 \times 10^{14}$ cm.

dimensional radiation-hydrodynamics with the development of Rayleigh–Taylor instabilities.

Jacobson-Galán et al. (2024b) favored the r1w6 model over the r1w5r model in their comparisons. The mass-loss rates of these two models are quite similar, and their early spectra are also very similar. Both models exhibit a higher ionization in the early stages than observed in SN 2024ggi. The early He II line in the r1w6 model is stronger than that in the r1w5r model, leading us to believe that the r1w5r model performs better in this aspect. Additionally, since the spectra of Jacobson-Galán et al. (2024b) do not extend beyond 10 days after the explosion, they did not observe the distinct P Cygni features that appeared later in SN 2024ggi. It is worth noting that the early-stage spectra of the r1w6 model (up to 14 days) also do not show this characteristic, making it inferior to the r1w5r model.

The r1w5r model is suitable for SN 2024ggi, as it can roughly reproduce the observed main IIn-like spectral features. However, the issue lies in the fact that the early ionization state of the model is too high. The CSM property of SN 2024ggi might be intermediate between r1w5r and r1w6. There may also be additional features ignored in D17, such as asymmetry, the breakup of the CDS, clumping in the CSM, and such. And the radiative transfer modeling could be improved. Therefore, the initial spectral evolution of SN 2024ggi provides a new opportunity for future development of spectroscopic models.

3.3. Evolution of Hydrogen Emission

In the early phase, when the SN photosphere is within the unshocked ionized CSM, the spectra are characterized by symmetric emission lines with narrow cores and extended, electron-scattering broadened wings. Figure A3 shows the double-component fitting of the early Hα emission of SN 2024ggi. Note that the broader wings are referred as midwidth components to distinguish them from the even wider emission lines in the later P Cygni profiles Doppler-broadened in the fast-expanding ejecta.

Based on the two-component fitting of Figure A3, we obtain the parameters and evolution of each component. To visually compare this evolution in Hα, we selected spectra taken by YFOSC+G14 in the first 3 days, as presented in the top panel of Figure 5, to minimize the influence of instrumental effects. All of these spectra are corrected for the redshift and rotation of the host galaxy; see more detail in Appendix A.2.

Given the low spectral resolution, an instrumental correction is necessary to accurately determine the FWHM of the Hα line via $\mathrm{FWHM}_{\mathrm{cor}} = (\mathrm{FWHM}^2_{\mathrm{obs}} - \mathrm{FWHM}^2_{\mathrm{inst}})^{1/2}$, where instrumental FWHM is estimated through the skyline O I λ6300.3. This method has been proved effective in the study of SN 2023ixf, where the value we obtained through midresolution spectra (Zhang et al. 2023) matches well with that from the high-resolution spectra (Smith et al. 2023), as seen in the middle panel of Figure 5. In this panel, the corrected FWHM of the narrow component broadens from about 50 km s^{-1} to approximately 200 km s^{-1} within hours on the first day. Initially, the $\mathrm{FWHM}_{\mathrm{obs}}$ is close to the instrumental $\mathrm{FWHM}_{\mathrm{inst}}$, making corrections potentially inaccurate. We propose 50 km s^{-1} as an upper limit of FWHM before radiation broadening, and the actual FWHM is likely narrower at $t < 14$ hr.

Despite a measurement uncertainty of around 50% in the third spectrum, there is a discernible broadening of spectral lines, indicating the onset of electron-scattering effects as well as the potential radiative acceleration of the unshocked CSM

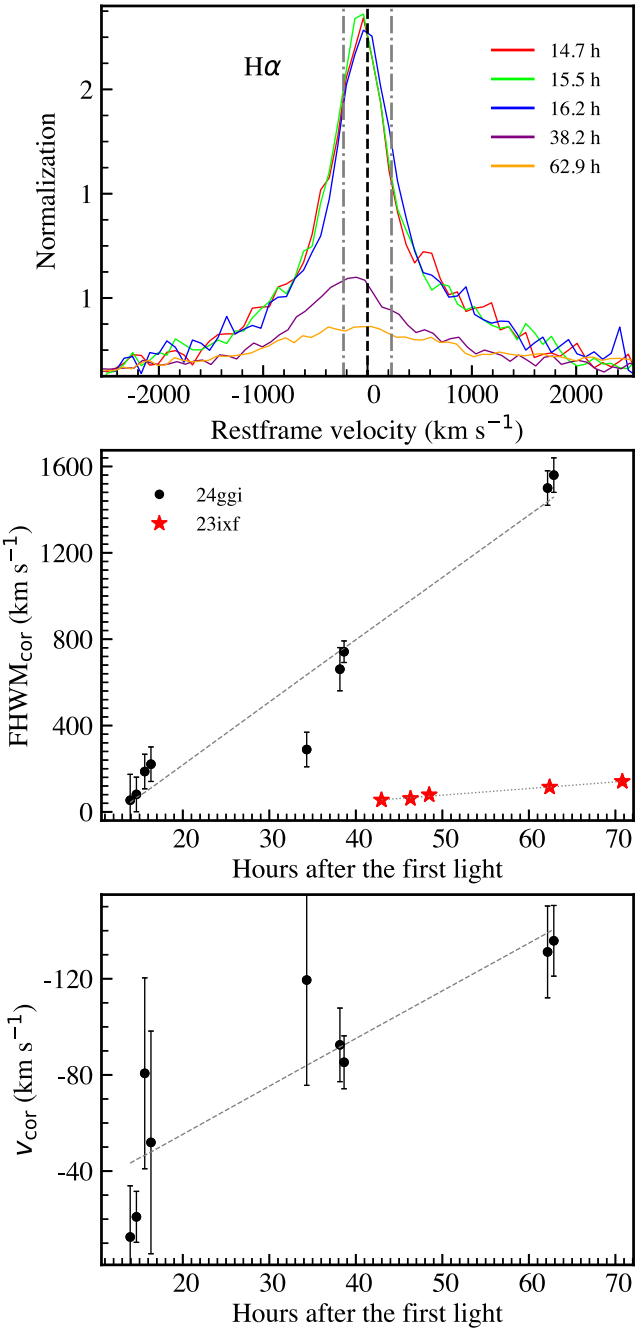

Figure 5. Top: Hα emission spectra of SN 2024ggi captured at $t < 3$ days obtained by LJT+YFOSC(G14). The black dashed line denotes the zero-velocity mark. The instrumental FWHM (460 km s^{-1}) of these spectra is indicated by the gray dotted–dashed lines. Middle: the evolution of the corrected FWHM of the narrow Hα component of SN 2024ggi compared with that of SN 2023ixf derived by the midresolution spectra of Zhang et al. (2023) and a high-resolution spectrum (at $t \approx 62.4$ hr) of Smith et al. (2023). Bottom: velocity evolution derived from the Hα emission of SN 2024ggi at $t < 3$ days. The dashed line represents a linear fit to the velocity data. The derived velocities have been corrected for skyline O I λ6300.3, as well as adjusted for the host galaxy's rotation at $v = -60 \pm 10$ km s^{-1}, which was determined through analysis of the Na I D absorption in midresolution spectra.

(D17). At this point, using the FWHM of the narrow lines to constrain the original CSM velocity becomes unfeasible.

Pessi et al. (2024) measured an FWHM ≈ 55 km s^{-1} of Hα at $t \sim 23.6$ hr (the epoch is calculated by the first light adopted in this Letter) with high-resolution spectroscopy. They found that this line broadened to 61 km s^{-1} 7 hr later. Their measurements indicate that although the low-resolution results are not precise enough, they can provide certain constraints at the earliest hours.

At $t \sim 38.7$ hr, a midresolution spectrum revealed that the FWHM of Hα had increased significantly, rendering instrumental broadening negligible. Remarkably, the narrow spectral lines of SN 2024ggi expanded to over 700 km s^{-1} within 48 hr. In contrast, the Hα FWHM of SN 2023ixf during a similar timescale after the first light was only 55 km s^{-1} ($t \sim 43$ hr; Zhang et al. 2023); see the middle panel of Figure 5. Furthermore, the broadening of the Hα narrow-line component in SN 2023ixf occurred much slower, increasing only from 55 to 140 km s^{-1} within the first 3 days and reaching close to 900 km s^{-1} when the narrow line was almost disappearing on the fifth day. Similarly to SN 2023ixf, the FWHM of the narrow Hα of SN 2020pni increased from 250 to nearly 1000 km s^{-1} in the first 5 days (Terreran et al. 2022). The more rapid and drastic broadening observed in SN 2024ggi suggests a less extended CSM than that of SN 2023ixf and SN 2020pni.

Although we cannot use the FWHM to limit the CSM velocity of SN 2024ggi, a noticeable blueshift was observed in the Hα emission. This shift is evident in the top panel of Figure 5, with precise measurements detailed in the middle panel. After some velocity adjustments and a refined wavelength calibration using the skyline O I λ6300.3, an initial blueshift velocity of -12 ± 20 km s^{-1} was measured at $t \sim 13.9$ hr. The resolution of the second spectrum at $t \sim 14.7$ hr is slightly higher, and the measured velocity is -20 ± 10 km s^{-1}. Considering the measurement errors in galactic rotation, the lower limit of the stellar wind velocity observed at the outer layer of CSM around SN 2024ggi is 20 ± 15 km s^{-1}. A fast expansion of the narrow Hα component was also seen in the SNe II with a short-lived IIn-like feature, e.g., SN 2020pni.

We averaged the measurements daily to reduce uncertainties, yielding mean velocities of 42 ± 29 km s^{-1}, 99 ± 23 km s^{-1}, and 133 ± 17 km s^{-1} in the first 3 days, respectively. These measures reveal the acceleration of the unshocked CSM by the radiation from the shock. The acceleration implies that the earlier observations can more genuinely reflect the movement of CSM before the explosion, representing the progenitor's stellar wind speed in its final phase. Thus, the inferred CSM velocity of SN 2024ggi does not exceed 40 km s^{-1}, consistent with the high-dispersion observation results (e.g., 37 km s^{-1}; Shrestha et al. 2024). Given the lower limit estimated before, the stellar wind velocity derived by our initial observation suggests that the progenitor wind velocity of SN 2024ggi is between 20 and 40 km s^{-1}.

4. Discussion

The initial spectral transformation and ionization processes observed in this SN provide a unique and valuable perspective into the final moments of a massive star. The rapid transition from IIn-like spectra to the photospheric phase in SN 2024ggi suggests that the fast-expanding ejecta quickly engulfed the CSM, and the CSM density decreased sharply at large distances.

Based on the preceding analysis, we have sketched the CSM of SN 2024ggi. The blueshifted Hα emission indicates a wind velocity of the outer CSM at 20 km s^{-1} $< v <$ 40 km s^{-1}. The comparison with the D17 model suggests a mass-loss rate at the

inner CSM on the order of 5×10^{-3}–$10^{-2}\,M_{\odot}\,\mathrm{yr}^{-1}$ to produce the observed IIn-like spectral features.

The duration and strength of the narrow emission lines depend on the radius and density of the CSM, providing valuable clues for the mass-loss rate of the progenitor. The narrow emission lines with electron-scattering broadened wings of SN 2024ggi vanished approximately 6 days after the explosion. Based on subsequent measurements of the hydrogen P Cygni absorption component, the maximum ejecta velocity of SN 2024ggi is 8000 km s^{-1}. Adopting this value, we can confidently infer that the distribution range of the CSM does not exceed 4×10^{14} cm. This aligns with the photosphere radius inferred from the bolometric luminosity on the sixth day, as seen in Figure A1. Considering the upper limit of the stellar wind speed of 40 km s^{-1}, it would take at least 3 yr for the stellar wind to reach that distance, but much longer if we adopt a slowly accelerating wind.

Comparison of SN 2024ggi with other SNe II exhibiting short-lived IIn-like spectra highlights the diversity in CSM properties. SN 2024ggi stands out for the fast transition from the IIn phase to the phase when spectral lines appear broad and dominated by Doppler broadening, which is consistent with a compact surrounding CSM. For example, SN 2024ggi has a more compact CSM than that of SN 2023ixf (e.g., with a CSM distribution region of 7×10^{14}; Zhang et al. 2023; Zimmerman et al. 2024) and SN 2018zd (e.g., with a CSM distribution region of 10^{15}; Zhang et al. 2020).

The analysis of the Hα emission line reveals significant broadening within 63 hr, and the FWHM increases from ∼50 to ∼1500 km s^{-1}, which is due to the radiative acceleration of the CSM. This is why the narrow component quickly disappears.

The early spectral (and photometric; S. Yan et al. 2024, in preparation) evolution of SN 2024ggi indicates that we caught the SN during the SBO. In particular, the four spectra taken between 13.9 and 16.2 hr showed spectra with lines of a low ionization level. Taking into account the influence of spectral resolution, it can be assumed that the spectral lines and blackbody temperature of these four spectra remained almost unchanged. Combined with the significant increase in ionization level observed in the 29.2 hr spectrum, it can be inferred that the SBO occurred during this period. The photosphere radius at this time was approximately 10^{14} cm. Subsequently, fluctuations in high-ionization lines were observed at 29.2 hr, 34.4 hr, and 38.2 hr, which may be related to the end of the SBO. The corresponding photosphere radius at this time was 1.5×10^{14} cm (Figure A1). In other words, the SBO of SN 2024ggi, as observed from the IIn-like spectrum, occurred within the region between 1×10^{14} and 1.5×10^{14} cm.

In summary, the study of SN 2024ggi will contribute to our understanding of the late stages of stellar evolution, the pivotal role of CSM in shaping the SN observations, the intriguing diversity of SNe II, and the process of shock-wave propagation in CSM.

Acknowledgments

This work is supported by the National Key R&D Program of China with No. 2021YFA1600404, the National Natural Science Foundation of China (12173082), the science research grants from the China Manned Space Project with No. CMS-CSST-2021-A12, the Yunnan Fundamental Research Projects (grants 202201AT070069 and 202401BC070007), the Top-notch Young Talents Program of Yunnan Province, the Light of West China Program provided by the Chinese Academy of Sciences, the International Centre of Supernovae, and Yunnan Key Laboratory (No. 202302AN360001). X.W. is supported by the National Natural Science Foundation of China (NSFC grants 12288102 and 1203300) and the Tencent Xplorer Prize. Y.-Z.C. is supported by the National Natural Science Foundation of China (NSFC; grant No. 12303054) and the Yunnan Fundamental Research Projects (grant No. 202401AU070063). Z.G. is supported by the ANID FONDECYT Postdoctoral program No. 3220029. This work was funded by ANID, Millennium Science Initiative, AIM23-0001. This work has made use of the University of Hertfordshire's high-performance computing facility (http://uhhpc.herts.ac.uk). L.W. is sponsored (in part) by the Chinese Academy of Sciences (CAS), through a grant to the CAS South America Center for Astronomy (CASSACA) in Santiago, Chile.

We acknowledge the support of the staff of the LJT, VLT, and TNG. Funding for the LJT has been provided by the CAS and the People's Government of Yunnan Province. The LJT is jointly operated and administrated by YNAO and the Center for Astronomical Mega-Science, CAS.

Facilities: YAO:2.4m, TNG, VLT:Antu, Magellan:Baade.

Software: PyRAF (Science Software Branch at STScI 2012), NumPy (Harris et al. 2020), Matplotlib (Hunter 2007), Astropy (Astropy Collaboration et al. 2013, 2018, 2022).

Appendix

A.1. Data Reduction

Figure 1 displays the spectra of SN 2024ggi obtained by LJT, TNG, and VLT UT1, with further specifics outlined in Table A1. All of these spectra are produced in the standard way in IRAF, including precise wavelength and flux calibration, and have been corrected for telluric absorption and redshift. The wavelength was double-checked by the skylines (e.g., O I λ5577.3, O I λ6300.3, and O I λ6363.8). The flux of the spectra was double-checked by the SED of *ugriz*-band photometry, as seen in Figure A1. During the spectroscopic monitoring of LJT, we got high-cadence photometry quasi-simultaneously. The flux of VLT and TNG are checked with the SED interpreted by the photometry of LJT and Burst Observer and Optical Transient Exploring System (S. Yan et al. 2024, in preparation). Figure A1 presents the bolometric light curve of SN 2024ggi based on the *ugriz*-band photometry and blackbody fitting. The temperature derived from the blackbody fitting and the photospheric radius estimated via luminosity and temperature are also plotted. We got one near-infrared spectrum from the Magellan telescope with FIRE (Folded-port InfraRed Echellette) on April 24, 2024 ($t \sim 14$ d), as seen in Figure A2, which was reduced with the FIREHOST V2.0 pipeline (Gagné et al. 2015).

Figure A3 displays two-components fitting of Hα emission in SN 2024ggi presented in spectra obtained in the first two days.

A.2. Na I D Absorption and Extinctions

We observed three sets of absorption lines in the midresolution spectrum of SN 2024ggi. Based on their wavelength relationships, we can infer that these three sets of lines are Na I D absorption lines from different redshifts, indicating dust extinction in the line-of-sight direction of SN 2024ggi, as seen in Figure A4. The first set at $z \sim 0.000036$ is the absorption

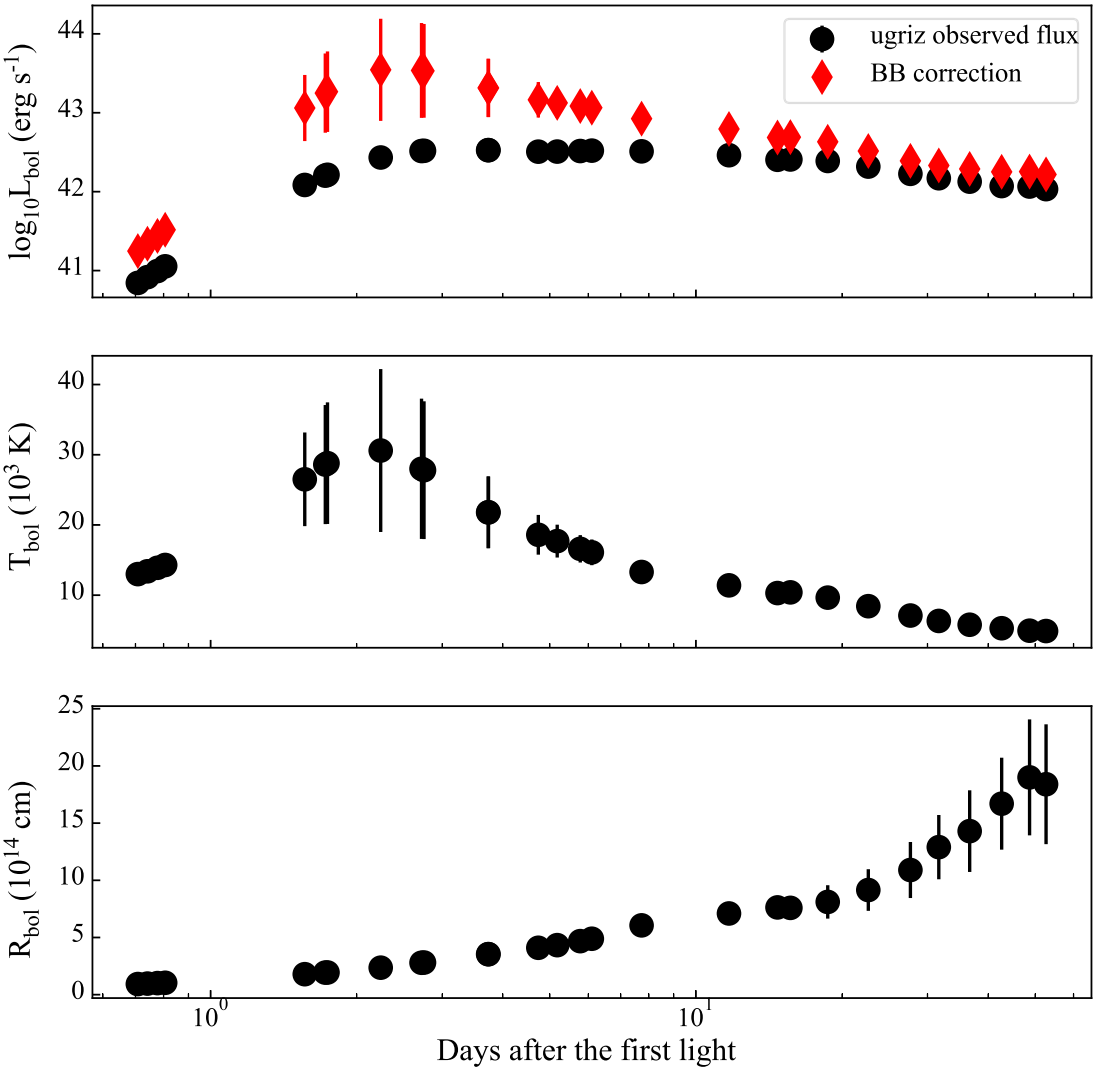

Figure A1. Bolometric light curve, blackbody temperature, and photospheric radius calculations for SN 2024ggi based on photometric data of LJT at the same time of spectral observation. Top panel: bolometric light curves determined through *ugriz*-band photometry and fitted to a blackbody curve. Middle panel: temperature determined from the blackbody fit of the photometry data. Bottom panel: photospheric radius determined using luminosity and temperature measurements.

from the Milky Way. Based on the redshift, $z \sim 0.00039$, the second set of absorption lines may originate from a molecular cloud within the Milky Way at a recession velocity of approximately 120 km s^{-1}. Given the redshift of NGC 3621 ($z = 0.002435 \pm 0.000007$; from NASA/IPAC Extragalactic Database), the third set of Na I D lines at $z \sim 0.002235$ should be from the host galaxy with a rotation velocity at -60 ± 10 km s^{-1}, where the velocity error is derived by the estimation of the skyline O I λ5577.3.

The EW of interstellar Na I D1 and D2 lines can be used to estimate the dust extinctions, e.g., the empirical relations in Poznanski et al. (2012). We derived the $E(B-V)$ of SN 2024ggi depending on the three sets of Na I D absorption, as listed in Table A2. The estimations from the same set of D1 and D2 are averaged. Based on this, we derived that the Galactic extinction is $E(B-V)_{\rm MW} = 0.048 \pm 0.009$ mag, which is close to the result of Schlafly & Finkbeiner (2011; i.e., $E(B-V)_{\rm MW} = 0.071$ mag). The extinctions of the host galaxy and the intermediate cloud are $E(B-V)_{\rm Host} = 0.063 \pm 0.005$ mag and $E(B-V)_{\rm IMC} = 0.050 \pm 0.009$ mag, respectively. Adopting the Galactic extinction of Schlafly & Finkbeiner (2011) and our host and intermediate cloud estimates, the total extinction of SN 2024ggi is $E(B-V) = 0.18 \pm 0.01$ mag, which is adopted in the related calculation of this paper. This measurement is consistent with the extinction results obtained by Pessi et al. (2024), i.e., $E(B-V) = 0.16 \pm 0.02$ mag, and Shrestha et al. (2024), i.e., $E(B-V) = 0.15 \pm 0.02$ mag, through high-dispersion spectroscopic observations of the Na I D lines.

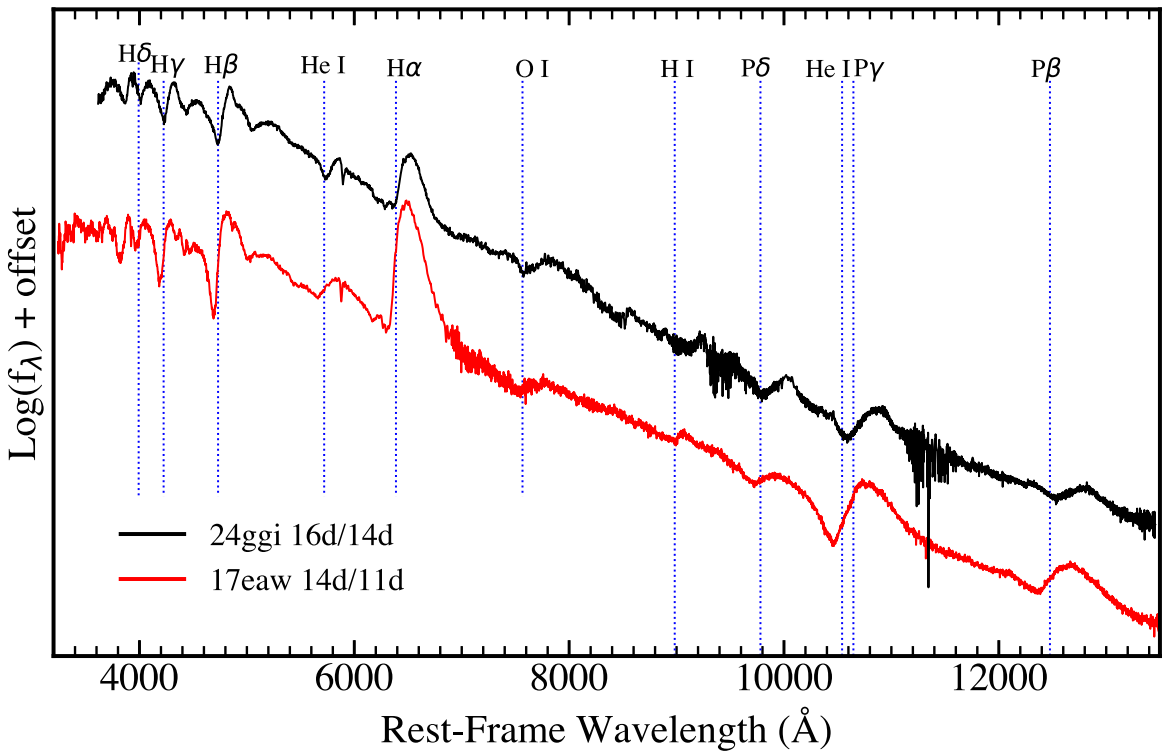

Figure A2. Optical-NIR spectrum of SN 2024ggi compared with SN 2017eaw (Szalai et al. 2019). The epoch of optical and NIR observation is marked after the name of each SN. The blue dotted line represents a blueshift corresponding to a velocity of -8000 km s^{-1}.

Table A1
Journal of Spectroscopic Observations of SN 2024ggi

Date (UT)	MJD	Epoch[a]	Range (Å)	Spec. Res.	Telescope+Inst.
Apr 11	60411.608	13.9 hr	3600–8800	410	LJT+YFOSC(G3)
Apr 11	60411.641	14.7 hr	3900–7600	650	LJT+YFOSC(G14)
Apr 11	60411.677	15.5 hr	3900–7600	650	LJT+YFOSC(G14)
Apr 11	60411.706	16.2 hr	3900–7600	650	LJT+YFOSC(G14)
Apr 11	60412.248	29.2 hr	3300–9200	370	VLT UT1+FORS2(300V)
Apr 11	60412.463	34.4 hr	3400–8100	410	TNG+LRB
Apr 12	60412.623	38.2 hr	3900–8870	650	LJT+YFOSC(G14)
Apr 12	60412.641	38.7 hr	3500–9500	3500	LJT+YFOSC(E9G10)
Apr 12	60413.141	50.7 hr	3300–9200	370	VLT UT1+FORS2(300V)
Apr 12	60413.151	50.9 hr	3600–5100	1200	VLT UT1+FORS2(1200b)
Apr 13	60413.620	62.2 hr	3500–9500	3500	LJT+YFOSC(E9G10)
Apr 13	60413.652	62.9 hr	3900–8870	650	LJT+YFOSC(G14)
Apr 14	60414.631	3.60 days	3400–9150	650	LJT+YFOSC(G14)
Apr 14	60414.638	3.61 days	3850–9160	410	LJT+YFOSC(G3)
Apr 15	60415.634	4.60 days	3400–9150	650	LJT+YFOSC(G14)
Apr 15	60416.078	5.05 days	3400–9300	370	VLT UT1+FORS2(300V)
Apr 16	60416.676	5.65 days	3850–9160	650	LJT+YFOSC(G14)
Apr 16	60416.989	5.96 days	3300–9200	370	VLT UT1+FORS2(300V)
Apr 16	60417.002	5.97 days	3600–5100	1200	VLT UT1+FORS2(1200b)
Apr 18	60418.627	7.60 days	3900–7600	650	LJT+YFOSC(G14)
Apr 22	60422.598	11.57 days	3900–8870	410	LJT+YFOSC(G3)
Apr 24	60424.980	13.95 days	8400–24000	6000	Magellan+FIRE
Apr 25	60425.626	14.60 days	3500–9500	3500	LJT+YFOSC(E9G10)
Apr 26	60426.554	15.52 days	3600–8800	410	LJT+YFOSC(G3)
Apr 29	60429.589	18.56 days	3900–7600	650	LJT+YFOSC(G14)
May 3	60433.557	22.53 days	3600–8800	410	LJT+YFOSC(G3)
May 8	60438.566	27.54 days	3600–8800	410	LJT+YFOSC(G3)
May 12	60442.556	31.53 days	3600–8800	410	LJT+YFOSC(G3)

Note.
[a] The epoch is relative to the first-light date, MJD = 60411.03.

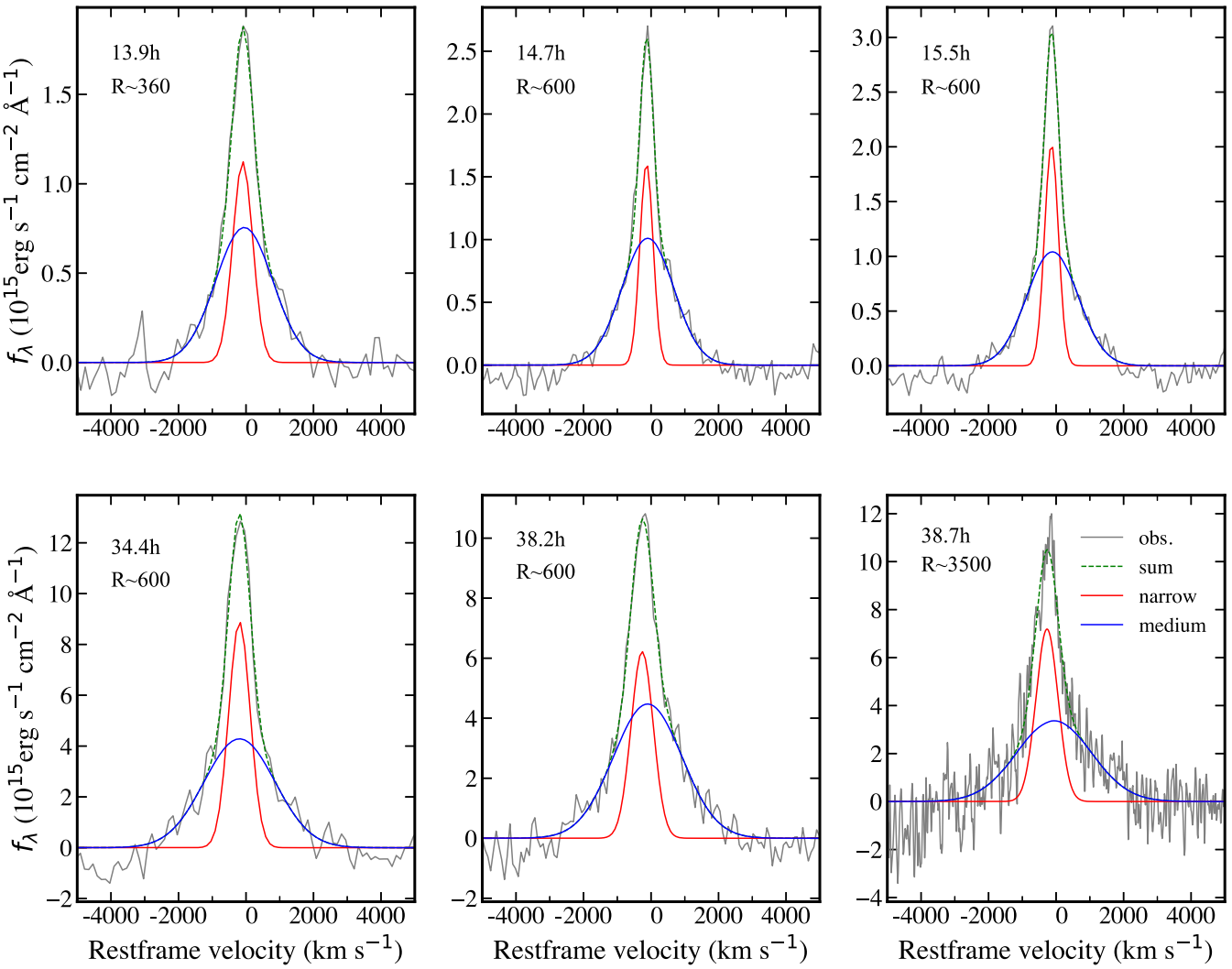

Figure A3. Gaussian and Lorentzian fits to the narrow and medium components of the Hα line in the spectra of SN 2024ggi at six selected phases. The spectral resolution of each spectrum is marked.

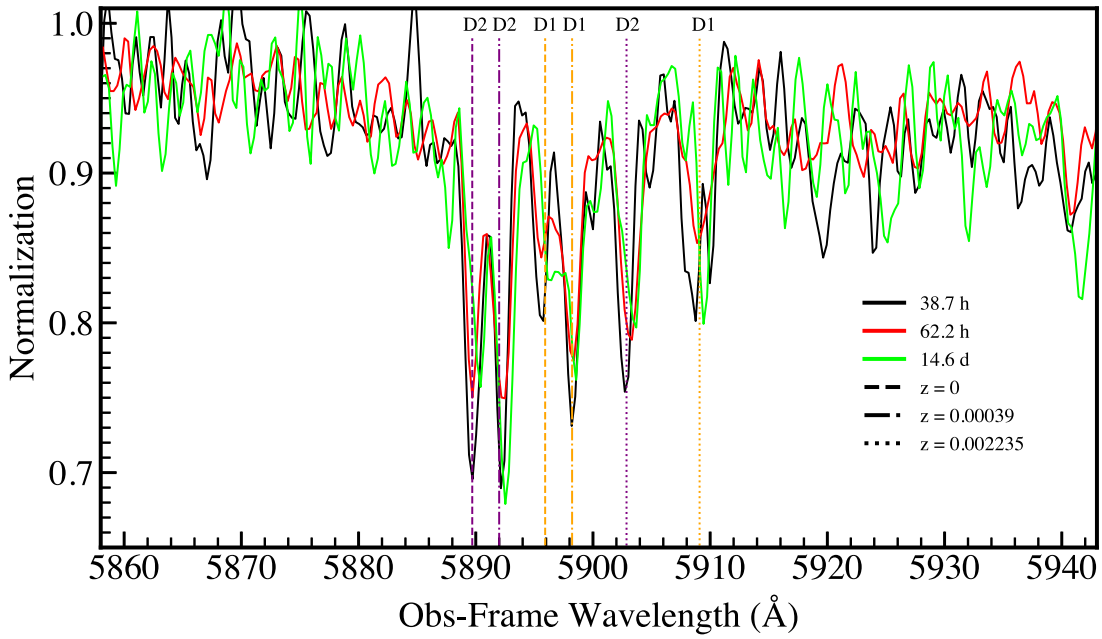

Figure A4. Three sets of Na I D absorption in the middle-resolution spectra of SN 2024ggi. The dashed, dashed–dotted, and dotted lines represent the Na I D at different redshifts as marked in the legend.

Table A2
Parameters of Na I D Lines and the Extinctions of SN 2024ggi

Line[a]	Obs. λ (Å)	$\Delta\lambda$ (Å)	EW (Å)	ΔEW (Å)	$E(B-V)$ (mag)	$\Delta E(B-V)$ (mag)
$D2_{MW}$	5889.91	0.24	0.30	0.03	0.053	0.006
$D2_{IMC}$	5892.30	0.21	0.33	0.01	0.064	0.000
$D1_{MW}$	5895.98	0.62	0.16	0.02	0.042	0.003
$D1_{IMC}$	5898.26	0.16	0.22	0.03	0.062	0.006
$D2_{Host}$	5903.08	0.28	0.25	0.01	0.043	0.001
$D1_{Host}$	5909.10	0.52	0.21	0.01	0.056	0.002

Note.
[a] MW represents the absorption from the Milky Way, IMC represents absorption from intermediate clouds, and Host represents absorption from the host galaxy.

ORCID iDs

Jujia Zhang https://orcid.org/0000-0002-8296-2590
Luc Dessart https://orcid.org/0000-0003-0599-8407
Xiaofeng Wang https://orcid.org/0000-0002-7334-2357
Yi Yang https://orcid.org/0000-0002-6535-8500
Zhen Guo https://orcid.org/0000-0003-0292-4832
Lingzhi Wang https://orcid.org/0000-0002-1094-3817
Zeyi Zhao https://orcid.org/0009-0005-2963-7245
Shengyu Yan https://orcid.org/0009-0004-4256-1209

References

Astropy Collaboration, Price-Whelan, A. M., Lim, P. L., et al. 2022, ApJ, 935, 167
Astropy Collaboration, Price-Whelan, A. M., Sipőcz, B. M., et al. 2018, AJ, 156, 123
Astropy Collaboration, Robitaille, T. P., Tollerud, E. J., et al. 2013, A&A, 558, A33
Bostroem, K. A., Pearson, J., Shrestha, M., et al. 2023, ApJL, 956, L5
Bruch, R. J., Gal-Yam, A., Schulze, S., et al. 2021, ApJ, 912, 46
Bruch, R. J., Gal-Yam, A., Yaron, O., et al. 2023, ApJ, 952, 119
Chen, T.-W., Yang, S., Srivastav, S., et al. 2024a, arXiv:2406.09270
Chen, X., Kumar, B., Er, X., et al. 2024b, arXiv:2405.07964
Chugai, N. N. 2001, MNRAS, 326, 1448
Dessart, L., & Hillier, D. J. 2006, A&A, 447, 691
Dessart, L., Hillier, D. J., Audit, E., Livne, E., & Waldman, R. 2016, MNRAS, 458, 2094
Dessart, L., Hillier, D. J., Yoon, S.-C., Waldman, R., & Livne, E. 2017, A&A, 603, A51
Fan, Y.-F., Bai, J.-M., Zhang, J.-J., et al. 2015, RAA, 15, 918
Fassia, A., Meikle, W. P. S., Chugai, N., et al. 2001, MNRAS, 325, 907
Filippenko, A. V. 1997, ARA&A, 35, 309
Fransson, C., Ergon, M., Challis, P. J., et al. 2014, ApJ, 797, 118
Gagné, J., Lambrides, E., Faherty, J. K., & Simcoe, R. A. 2015, FireHose_v2: Firehose v2.0, Zenodo, doi:10.5281/zenodo.18775
Gal-Yam, A. 2017, in Handbook of Supernovae, ed. A. W. Alsabti & P. Murdin (Berlin: Springer), 195
Gal-Yam, A., Arcavi, I., Ofek, E. O., et al. 2014, Natur, 509, 471
Hamuy, M., Pinto, P. A., Maza, J., et al. 2001, ApJ, 558, 615
Harris, C. R., Millman, K. J., van der Walt, S. J., et al. 2020, Natur, 585, 357
Heger, A., Fryer, C. L., Woosley, S. E., Langer, N., & Hartmann, D. H. 2003, ApJ, 591, 288
Hiramatsu, D., Howell, D. A., Van Dyk, S. D., et al. 2021, NatAs, 5, 903
Hiramatsu, D., Tsuna, D., Berger, E., et al. 2023, ApJL, 955, L8
Hunter, J. D. 2007, CSE, 9, 90
Jacobson-Galán, W. V., Dessart, L., Davis, K. W., et al. 2024a, arXiv:2403.02382
Jacobson-Galán, W. V., Davis, K. W., Kilpatrick, C. D., et al. 2024b, arXiv:2404.19006
Jacobson-Galán, W. V., Dessart, L., Jones, D. O., et al. 2022, ApJ, 924, 15
Kanbur, S., Ngeow, C., Nikolaev, S., Tanvir, N., & Hendry, M. 2003, A&A, 411, 361
Leonard, D. C., Filippenko, A. V., Barth, A. J., & Matheson, T. 2000, ApJ, 536, 239
Leonard, D. C., Filippenko, A. V., Gates, E. L., et al. 2002, PASP, 114, 35
Li, G., Hu, M., Li, W., et al. 2024, Natur, 627, 754
Niemela, V. S., Ruiz, M. T., & Phillips, M. M. 1985, ApJ, 289, 52
Pessi, T., Cartier, R., Hueichapan, E., et al. 2024, arXiv:2405.02274
Poznanski, D., Prochaska, J. X., & Bloom, J. S. 2012, MNRAS, 426, 1465
Schlafly, E. F., & Finkbeiner, D. P. 2011, ApJ, 737, 103
Schlegel, E. M. 1990, MNRAS, 244, 269
Science Software Branch at STScI 2012, PyRAF: Python Alternative for IRAF, Astrophysics Source Code Library, ascl:1207.011
Shivvers, I., Groh, J. H., Mauerhan, J. C., et al. 2015, ApJ, 806, 213
Shrestha, M., Bostroem, K. A., Sand, D. J., et al. 2024, arXiv:2405.18490
Smith, N., Pearson, J., Sand, D. J., et al. 2023, ApJ, 956, 46
Szalai, T., Vinkó, J., Könyves-Tóth, R., et al. 2019, ApJ, 876, 19
Tartaglia, L., Pastorello, A., Sollerman, J., et al. 2020, A&A, 635, A39
Tartaglia, L., Sand, D. J., Groh, J. H., et al. 2021, ApJ, 907, 52
Terreran, G., Jacobson-Galán, W. V., Groh, J. H., et al. 2022, ApJ, 926, 20
Terreran, G., Jerkstrand, A., Benetti, S., et al. 2016, MNRAS, 462, 137
Tonry, J., Denneau, L., Weiland, H., et al. 2024, TNSTR, 2024-1020, 1
Wang, C.-J., Bai, J.-M., Fan, Y.-F., et al. 2019, RAA, 19, 149
Waxman, E., & Katz, B. 2017, in Handbook of Supernovae, ed. A. W. Alsabti & P. Murdin, 967
Xiang, D. F., Mo, J., Wang, X. F., et al. 2024, ApJL, 969, L15
Yaron, O., Perley, D. A., Gal-Yam, A., et al. 2017, NatPh, 13, 510
Zhai, Q., Li, L., Wang, Z., Zhang, J., & Wang, X. 2024, TNSAN, 104, 1
Zhang, J., Lin, H., Wang, X., et al. 2023, SciBu, 68, 2548
Zhang, J., Wang, X., József, V., et al. 2020, MNRAS, 498, 84
Zhang, T., Wang, X., Wu, C., et al. 2012, AJ, 144, 131
Zimmerman, E. A., Irani, I., Chen, P., et al. 2024, Natur, 627, 759